Research Article Vol. 33, No. 12 / 16 Jun 2025 / Optics Express 26578

Optics EXPRESS

Monolithic X-ray achromat

PENG QI,[1,*] UMUT TUNCA SANLI,[1,2] SHUAI ZHAO,[1,3] GRIFFIN RODGERS,[4] GEORG SCHULZ,[4] MANO RAJ DHANALAKSHMI VEERARAJ,[1] MARIE-CHRISTINE ZDORA,[1,5] BERT MÜLLER,[4] ANA DIAZ,[6] DARIO FERREIRA SANCHEZ,[7] DANIEL GROLIMUND,[7] MARIO SCHEEL,[8] TIMM WEITKAMP,[8] CHRISTIAN DAVID,[1] AND JOAN VILA-COMAMALA[1]

[1] *Laboratory for X-ray Nanoscience and Technologies, Paul Scherrer Institute, 5232 Villigen PSI, Switzerland*
[2] *Present address: KNF Holding AG, 8600 Dübendorf Zürich, Switzerland*
[3] *National Synchrotron Radiation Laboratory, University of Science and Technology of China, 230029 Hefei, China*
[4] *Department of Biomedical Engineering, University of Basel, 4003 Basel, Switzerland*
[5] *Present address: School of Physics and Astronomy, Monash University, 3800 Clayton VIC, Australia*
[6] *Laboratory for Macromolecules and Bioimaging, Paul Scherrer Institut, 5232 Villigen PSI, Switzerland*
[7] *Laboratory for Synchrotron Radiation and Femtochemistry, Paul Scherrer Institut, 5232 Villigen PSI, Switzerland*
[8] *Synchrotron SOLEIL, L'Orme des Merisiers, Départementale 128, 91190 Saint-Aubin, France*
[*] *peng.qi@psi.ch*

Abstract: X-ray imaging techniques employing diffractive and refractive lenses face the challenge of chromatic aberration if X-ray beams with a broad photon energy range are used. Recent advances combining a compound refractive lens and a Fresnel zone plate have enabled the development of achromatic lenses for X-rays, which exhibit a constant focal length over a wider range of photon energies. However, in this first demonstration, the potential of the achromatic X-ray lens was limited by the challenging task of aligning the two individual separate components. In this investigation, we designed, fabricated, and characterized monolithic X-ray achromatic lenses by integrating a Fresnel zone plate and a compound refractive lens onto a single substrate. This innovative approach inherently achieves precise alignment during fabrication, greatly simplifying and stabilizing the alignment for the X-ray imaging setups. Benefiting from an increased numerical aperture, the reported monolithic lens demonstrated state-of-the-art achromatic focusing down to approximately 200 nm for photon energies ranging from 6.6 keV to 7.7 keV. With these advancements, we present the first successful application of an achromatic lens in scanning and full-field transmission X-ray microscopy, as well as fluorescence spectroscopy, highlighting its potential for broad adoption across diverse X-ray imaging applications.

1. Introduction

The chromatic aberration of refractive and diffractive lenses has been a long-standing challenge in X-ray focusing and X-ray imaging if photon beams with a broad X-ray energy spectrum are used [1,2]. In the visible regime achromatic doublets are realized by combining divergent and convergent refractive lenses made of materials of different dispersion which measures the change of the refractive index as a function of the wavelength. For X-rays, this method cannot be applied because the difference in dispersion between any two materials is insufficient to realize

#557328 https://doi.org/10.1364/OE.557328
Journal © 2025 Received 31 Jan 2025; revised 14 May 2025; accepted 16 May 2025; published 13 Jun 2025

the correction of the chromatic aberration, except for the very specific case of exploiting the anomalous dispersion near the absorption edges of the refractive lens material [3].

An alternative approach to realizing an achromatic X-ray lens involves combining a divergent refractive lens with a convergent diffractive lens, as theoretically described in the past [4,5]. The difference in the dispersion of the two lens types enables the cancellation of the chromatic aberration at a specific photon energy range, provided that the focusing powers of the compound refractive lens (CRL) [6] and the Fresnel zone plate (FZP) [7] are carefully selected. Recently, the first successful realization of X-ray achromat was demonstrated for X-rays with energies ranging from 5.8 keV to 7.3 keV [8].

This advancement offers two key advantages for X-ray imaging techniques. Firstly, it benefits methods that prioritize higher intensity over monochromaticity by enabling the focusing of polychromatic X-rays without suffering from chromatic aberration. Secondly, it simplifies X-ray spectroscopy investigations requiring variable energy measurements, as the achromat maintains a constant focal position across the energy range, thus eliminating the need to adjust the sample-lens distance during energy scans. This novel X-ray optical component is poised to significantly enhance the experimental throughput of X-ray imaging techniques. A subsequent development of an apochromat further broadened the energy range of achromatic correction to 5 keV [9].

In the past implementation of an X-ray achromat and apochromat [8,9], the two individual elements were supported by separate support membranes. The quality of the achromatic X-ray focusing was hindered by the challenges and accuracy of aligning the two separate components. The multiple degrees of freedom in their relative positioning can easily result in spatial and angular misalignment between the two elements and lead to distortions of the focusing spot and reduced imaging performance [10,11].

In this study, we developed, fabricated and characterized a monolithic design of the achromatic X-ray lens, in which the FZP and CRL are supported on the same silicon nitride membrane. This fabrication approach ensures that the relative position and angle of the elements are accurately prealigned and fixed with a precision on the order of 100 nm. This is accomplished with mix-and-match lithography, wherein the CRL is produced on the top of the FZP on the same chip, as illustrated in Fig. 1. The FZP was fabricated using high-resolution electron-beam lithography and gold electroplating [12,13], while the CRL was 3D printed employing two-photon polymerization [14,15]. The accurate alignment between the two components was realized during the start of the CRL 3D printing.

As a result, the use of monolithic achromatic lenses at an X-ray imaging setup requires only the alignment with respect to the X-ray beam. This strategy significantly reduces the system's alignment complexity and stability requirements. Compared to an achromat composed of two separate elements, the monolithic achromatic lens reduces the alignment degrees of freedom from 6 (two for the relative spatial alignment between elements, plus two angular alignment for each element) down to 2 (angular alignments relative to the X-ray beam). Consequently, the alignment process achieves improved accuracy and precision while requiring considerably less effort. More importantly, alignment stability is significantly enhanced, becoming robust against unsynchronized adjustment between the two elements and positional drifts over time. In the following sections, we describe in detail the novel fabrication approach and demonstrate a higher performance of the monolithic achromat achieving a focal spot of 200 nm. Furthermore, We illustrate the applicability of such lenses in full-field and scanning transmission X-ray microscopy, as well as spectroscopy applications.

Optics EXPRESS

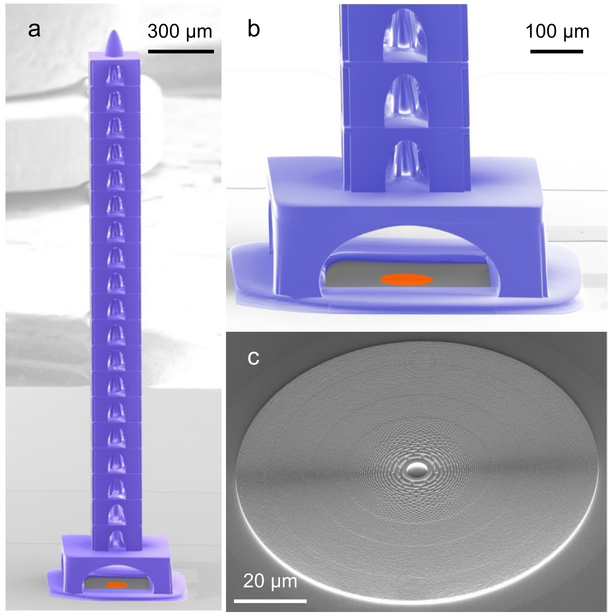

Fig. 1. Scanning electron microscopy images of the monolithic achromatic X-ray lens: (a) overview of the entire structure, (b) zoomed-in view of the CRL footing, showing the FZP, in orange, accurately centered below the CRL in blue, and (c) close-up view of the gold FZP.

2. Results

2.1. Design of the monolithic achromat

The monolithic achromatic X-ray lens was designed following the procedure reported in Kubec (2022) [8], combining a convergent FZP and a divergent CRL to achieve achromatic focusing over a photon energy range centered around 7.1 keV. In the specific case that the separation between the FZP and CRL approaches zero, the focal length's linear dependence on energy variation disappears at [8]

$$f_{\mathrm{CRL}} = -2f_{\mathrm{FZP}}. \tag{1}$$

As a result, the focal distance, f_{A}, as a function of energy change, $\Delta E/E_0$, follows the formulation [8],

$$\begin{aligned} f_{\mathrm{A}} &= 2f_{\mathrm{FZP}}\left[1-\sum_{k=0}^{\infty}(-1)^{k+1}2^k\left(\frac{\Delta E}{E_0}\right)^{k+2}\right] \\ &= 2f_{\mathrm{FZP}}\left[1+\left(\frac{\Delta E}{E_0}\right)^2-2\left(\frac{\Delta E}{E_0}\right)^3+4\left(\frac{\Delta E}{E_0}\right)^4-8\left(\frac{\Delta E}{E_0}\right)^5+16\left(\frac{\Delta E}{E_0}\right)^6-32\left(\frac{\Delta E}{E_0}\right)^7+\dots\right], \end{aligned} \tag{2}$$

where the quadratic term becomes dominant, E_0 is the design energy. Figure 2(a) shows the focal spot position of the achromatic X-ray lens along the optical axis as a function of X-ray energy, compared to the expected behavior for an FZP of the same focal length at the design energy.

More in detail, the FZP has a diameter of 100 µm and an outermost zone width of 83 nm, providing a focal length of $f_{\mathrm{FZP}} = 47.5$ mm at the central design energy, 7.1 keV. The divergent CRL consisted of 20 identical stacked refractive lenses with an aperture of 100 µm, a height of 125 µm and a radius of curvature at the vertex of the parabola of 20 µm. The total height of the refractive structure was 2.5 mm. It has a virtual focal length of $f_{\mathrm{CRL}} = -95$ mm at the central

Optics EXPRESS

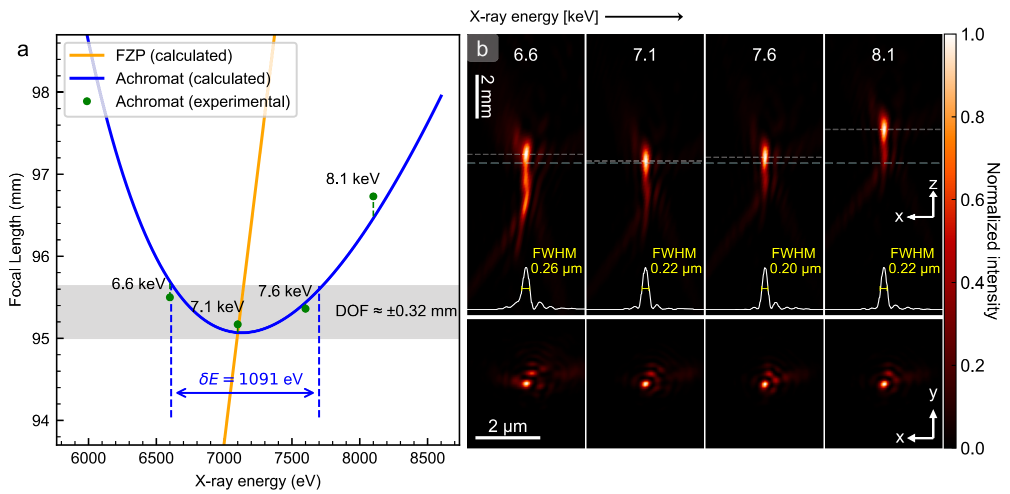

Fig. 2. Characterization of the monolithic achromat. (a) The focal length of the designed achromat and a comparison Fresnel zone plate as a function of energy, as well as the measured focal lengths of the achromat at multiple energies. (b) The ptychography reconstructions of the focal spot delivered by the monolithic X-ray achromat for photon energies ranging from 6.6 keV to 8.1 keV. The top row illustrates the propagation of the X-ray beam along the optical axis (z-axis), while the bottom row shows the intensity of the propagated focal spot from the sample position. Cross section intensity profiles at the focal positions indicated by the dashed white lines are also shown, as well as the sample position during the ptychography scan indicated by the dashed cyan line. Data were acquired at the cSAXS beamline at SLS.

photon energy, and it matches the achromat condition (Eq. (1)) with the chosen FZP parameters. The resulting achromatic focal length of the combination of the FZP and the CRL is

$$f_A = 2f_{FZP} = -f_{CRL} = 95 \text{ mm}$$

at 7.1 keV. With these given parameters, the monolithic X-ray achromat is expected to deliver a diffraction-limited focal spot size of approximately 200 nm with a depth of focus of ±0.32 mm, featuring an achromatic range of approximately 1.1 keV.

The realization of the monolithic X-ray achromat critically relies on the compatibility of the fabrication methods of both components on a single substrate. The FZP was fabricated combining high-resolution electron-beam lithography (EBL) and gold electroplating [12] on a silicon nitride membrane substrate. After that, the CRL was fabricated by two-photon polymerization 3D printing right on top of the FZP on the same substrate. Before printing the CRL structure, the position of the FZP on the membrane was identified using the built-in light microscope of the 3D printer, equipped with a 63× objective lens. The central zones of the FZP were used as a reference marker for printing the CRL. Although the spatial resolution of the microscope is limited by the wavelength of visible light, the center of a structure larger than the spatial resolution can be determined to a much better precision [16,17]. With the built-in microscope in Nanoscribe PPGT+, the obtained alignment precision is on the order of 100 nm. In addition, the supporting structure of the stacked refractive lenses was designed to ensure the robustness of the whole 3D-printed assembly. The scanning electron microscopy (SEM) images in Fig. 1(a) and (b) provide an overview of the high-aspect ratio monolithic X-ray achromat. The FZP (in orange) is well aligned under the CRL (in blue), both positioned on the top of the 250 nm-thick silicon nitride membrane. Figure 1(c) shows a closer view of the gold FZP. At 7.1 keV, the combined efficiency of the monolithic achromat is expected to be around 10% - see Method section.

2.2. Characterization of the achromatic behavior

Ptychographic imaging and scanning transmission X-ray microscopy (STXM) experiments were performed from 6.6 keV to 8.1 keV at the cSAXS beamline [18,19] at the Swiss Light Source (SLS) to characterize the achromatic capabilities and focusing performance of the monolithic X-ray achromat. The achromat was used to provide the focal spot both used for ptychography and STXM measurements. For these experiments, a Siemens star made of 750 nm tall gold structures with innermost spoke width of 50 nm was used as the test sample.

X-ray ptychography is an imaging technique that simultaneously provides absorption and phase contrast images of the sample with a spatial resolution that is not limited by a lens [20], and it also allows reconstruction of complex-valued illumination [18]. This capability makes X-ray ptychography an ideal technique to characterize X-ray optics [21], as the reconstructed illumination can be propagated to different points along the optical axis to investigate the focusing behavior of the lens.

The ptychographic reconstructions of the focal spot of the monolithic X-ray achromat over the photon energy range from 6.6 keV to 8.1 keV are shown in Fig. 2(b). For energies within the achromatic range, the change in focal distance remains within the depth of focus, as predicted. The lower panels display the intensity of the focused beam at the focal plane, while the upper panels show the propagation of the X-ray beam along the optical axis z. The FWHMs of the focal spots are about 200 nm, which matches the expected diffraction-limited resolution value for monolithic X-ray achromat. More details on the ptychographic reconstruction can be found in the Experiments section and Supplement 1 Figure S1.

In STXM, the sample is placed in the focal plane of a focusing lens, then raster-scanned to produce pixel-by-pixel transmission or differential phase contrast images, where the spatial resolution is limited to the focal spot size delivered by the focusing lens [22]. Here we report on STXM measurements based on the transmitted intensity. The STXM image shown in Fig. 3(a), which was acquired by the monolithic X-ray achromat, demonstrates that the 200 nm spokes of a Siemens star, marked by the innermost ring, are resolved. It shows significantly higher quality compared to the STXM image acquired with an achromat composed of two separated components [8] shown in Fig. 3(b). The enhancement can be attributed to two main factors. Firstly, the monolithic achromat was designed with twice the numerical aperture of its predecessor, effectively improving the diffraction-limited resolution by a factor of two. Secondly, the spoke bending observed in the doublet achromat (Fig. 3(b)) is no longer present when the monolithic lens is used (Fig. 3(a)), consistent with the alignment and stability improvements enabled by the monolithic X-ray achromat design. However, a direction-dependent blur exists in both images, which we attribute to the side lobe of the probes as shown in Fig. 2(b).

Full-field transmission X-ray microscopy (TXM) [23,24] was performed using the monolithic X-ray achromat as the objective lens at the experimental station of the ANATOMIX beamline at Synchrotron SOLEIL (France) [25]. Monochromatic X-rays with photon energies ranging from 6.6 keV to 8.1 keV were used to image a Siemens star pattern etched into a 500 nm thick tantalum layer, with an innermost spoke width of 50 nm. The TXM setup was initially aligned and focused at 7.1 keV, the central photon energy of the monolithic X-ray achromat. Then, consecutive TXM images were taken without modifying the distance between the sample and monolithic achromat, that is, without refocusing, at photon energies of 6.6, 7.1, 7.6 and 8.1 keV, as shown in Fig. 4.

As expected from the achromatic behavior, the TXM images at 7.1 keV and 7.6 keV look in focus and of similar quality, while the TXM image at 8.1 keV is out of focus. Additionally, at 6.6 keV, an increase in noise was observed in the resulting TXM image, primarily due to higher X-ray absorption in the CRL at this lower energy. The non-uniform contrast in the field of view visible in the TXM images is mainly attributed to two different factors. First, the CRL stack used in the TXM experiments suffered from deformations during the irradiation (see Supplement 1 Figure S2 for details). The supporting structure of the CRL stack used in these initial attempts

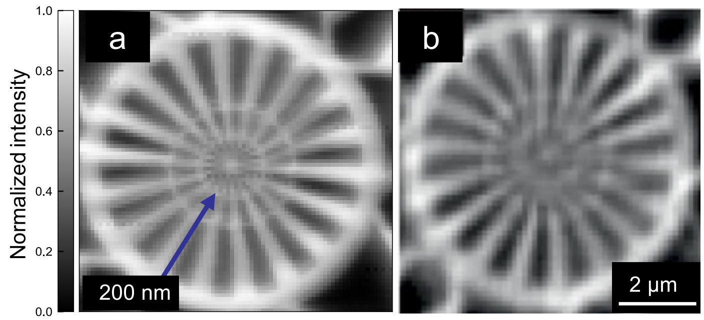

Fig. 3. Comparison of the STXM images of the same Siemens star pattern, collected with (a) the monolithic X-ray achromat at its design energy 7.1 keV and (b) an X-ray achromat composed of separate individual elements [8] at its design energy 6.2 keV. The width of the spokes at the innermost ring of the Siemens star is 200 nm. The monolithic X-ray achromat demonstrates superior imaging quality compared to its predecessor. Data acquired at the cSAXS beamline at SLS.

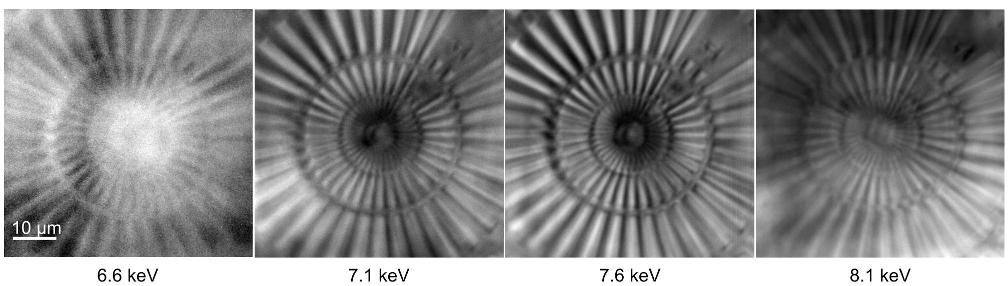

Fig. 4. Full-field TXM images of a Siemens star pattern acquired using the monolithic X-ray achromat as objective lens at photon energies ranging from 6.6 keV to 8.1 keV, presented in a linear gray scale indicating intensity from low (black) to high (white). The TXM images at different photon energies were taken consecutively without modifying the sample to achromat distance. The data was collected at the ANATOMIX beamline at Synchrotron SOLEIL.

for realizing the monolithic lens was less stable than the final strengthened form shown in Fig. 1 used for scanning microscopy experiments. Second, the TXM experimental setup for these measurements lacked motorized stages, and the tilt alignment of the monolithic achromat in respect to the X-ray beam was performed manually, which was far from optimal and likely contributed to the non-uniform contrast of the TXM images. This alignment limitation has been addressed in other presented experiments by employing the required tilt alignment hardware and procedures. Nevertheless, these results demonstrate the first ever implementation of an achromatic X-ray lens for full-field TXM.

2.3. Applications in X-ray absorption spectroscopy and fluorescence imaging

Several measurements were conducted at the microXAS beamline [26] of the SLS to demonstrate the capabilities of the monolithic X-ray achromat for X-ray absorption spectroscopy and fluorescence imaging [27]. A monochromatic X-ray beam, with photon energy ranging from 7.0 keV to 8.6 keV, was focused on the sample by the monolithic X-ray achromat. Then, the sample was raster-scanned while collecting both transmission and fluorescence signals. For the fluorescence measurements, a microfabricated sample containing Fe, Co and Ni structures

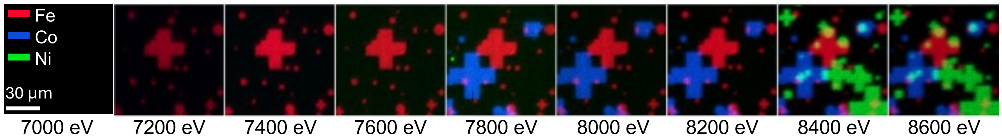

Fig. 5. X-ray fluorescence images acquired between 7.0 keV and 8.6 keV for a lithographically fabricated sample containing Fe, Co, and Ni structures. The fluorescence signals of the three elements were acquired using different channels of a silicon drift detector. Data were collected at the microXAS beamline at SLS.

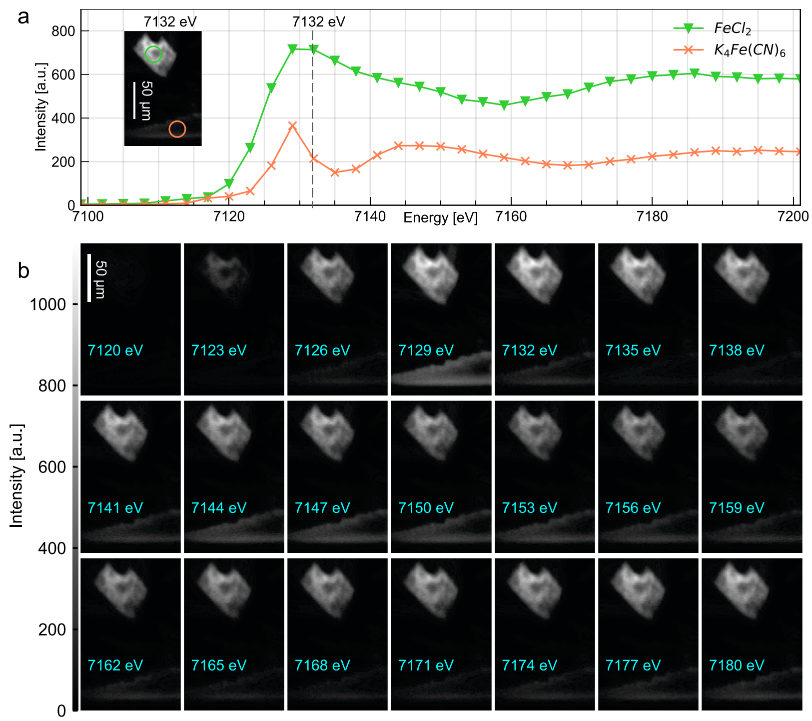

Fig. 6. X-ray fluorescence measurements of a sample containing $FeCl_2$ and $K_4Fe(CN)_6$ salts, conducted without mechanical refocusing of the lens. (a) X-ray absorption near edge structure (XANES) spectra from 7100 eV to 7200 eV recorded in fluorescence mode at two regions with accumulated $FeCl_2$ and $K_4Fe(CN)_6$ as marked with color-coded circles. (b) Fluorescence intensity shown in linear gray scale from 7120 eV to 7180 eV. Data were collected at the microXAS beamline at SLS.

was used. This sample was produced through a multi-step process involving electron-beam lithography, metal evaporation and lift-off. The initial focusing was done at a photon energy just above the Fe K-edge (7112 eV). Then, fluorescence signals were acquired at consecutively higher energies until going above the absorption K-edges of Fe, Co and Ni. The images were acquired without any refocusing or adjustment of the distance between the monolithic X-ray achromat and the sample. As shown in Fig. 5, the fluorescence images maintain high quality across the broad photon energy range, with only the image collected at 8600 eV exhibiting a slight defocused blur.

Additionally, X-ray absorption spectra near the Fe K-edge were collected in fluorescence mode over a 100 eV energy range in steps of 3 eV, using a sample containing $FeCl_2$ and $K_4Fe(CN)_6$, each exhibiting different Fe oxidation states. As depicted in Fig. 6, the spectral curves measured

Optics EXPRESS

at the color-coded circles clearly identify the two compounds. The higher intensity curve, along with the overall brighter region, indicates a higher concentration of $FeCl_2$. Both examples demonstrate the capability of the monolithic X-ray achromat for applications requiring energy scanning without mechanical refocusing. This represents the first-ever realization of X-ray spectroscopic measurements using an X-ray achromatic lens.

3. Discussion

The realization of the achromatic X-ray lens as a monolithic device represents a significant advancement compared to its earlier implementation, which relied on two separate individual optical components [8]. Our approach introduces a previously unexplored concept by integrating fundamentally distinct fabrication techniques into a single, monolithic design. In particular, several technical developments have been key to achieving superior performance of the new optical device. First, the CRL support structure was redesigned to enhance robustness and enable the fabrication of taller polymer structures, which are essential to realize achromatic X-ray lenses with higher focusing power, see Supplement 1 Figure S2. Second, accurate and stable alignment between the FZP and CRL was achieved during the 3D printing step. Finally, the FZP was fabricated on a silicon chip with a small silicon nitride membrane, allowing the CRL support footing to be printed directly onto the silicon frame, thereby bypassing the challenges associated with directly 3D printing on the fragile membrane.

Overall, the integration of the FZP and CRL on a single monolithic device greatly simplifies the alignment procedures in the X-ray setup and overcomes the inherent mechanical stability limitations of the preceding implementation of the achromatic X-ray lens that combined two separate elements. Our experimental characterization shows that the monolithic X-ray achromat provides high-resolution achromatic imaging with a spatial resolution down to 200 nm, along with improved imaging quality. Currently, our monolithic X-ray achromats are suitable to operate at photon energies between 6.0 keV and 12.0 keV, with an effective achromatic correction range of approximately 1.1 keV around the design energy. Our experimental results also showcase the first applications of the achromatic X-ray lens in full-field TXM, as well as elemental and chemical imaging. Altogether, our findings prove that achromatic X-ray lenses can now be designed and fabricated as a single optical device, which holds great potential for enhancing X-ray focusing and imaging methods. Future work will focus on optimizing the achromatic lens design towards higher resolution and photon energies. In both cases, maintaining reasonable efficiencies is the main challenge. The fabrication of the diffractive part – meaning the Fresnel zone plate – has already been well developed towards these directions using advanced nanolithography techniques [28–31], However, providing a refractive lens with sufficiently high (defocusing) refractive power requires even taller structures than the ones presented here, leading to high absorption losses. Here, optimized profiles of the refractive structures need to be applied to minimize the required height and improve the transmission [32].

As the development of achromatic X-ray lenses advances, we anticipate their increasing impact in the fields of X-ray microscopy and spectroscopy, benefiting scientific applications for both accelerator-based and laboratory X-ray sources.

4. Methods

4.1. FZP fabrication

The Fresnel zone plate of the monolithic X-ray achromat was fabricated on a silicon chip with a 250 nm thick Si_3N_4 membrane window with dimensions of $160 \times 160\ \mu m^2$. A layer of 5 nm Cr first evaporated onto the membrane, followed by the deposition of a layer of 20 nm Au. The electron-beam resist was spin-coated from an 8% 950k PMMA solution in anisole at 1500 rpm for 60 seconds and subsequently baked at 175° for 3 minutes. The FZP pattern was then exposed onto the resist using a 100 kV electron-beam with a Vistec EBPG 5000+ system. Following exposure, the pattern was developed in a mixture of isopropyl alcohol (IPA) and H_2O in a 7:3 ratio, and then cleaned with O_2 plasma. The gold structure was formed through electroplating, and the remaining resist was removed with acetone.

The fabricated FZP has a diameter of 100 µm and an outermost zone width of 83 nm, with a gold structure thickness of 1150 nm. The first-order diffraction efficiency at the design energy of 7.1 keV is estimated to be 27.5%, and the high quality of the zone plate structures suggests that the actual efficiency is close to that value.

4.2. CRL fabrication

The CRL was designed using OpenSCAD software and fabricated with a commercially available two-photon polymerization (2PP) 3D printing system, the Photonic Professional GT+ (Nanoscribe, Germany) [33]. Both the CRL and the FZP were produced on the same silicon chip. However, the gold-coated silicon nitride membrane substrate presented challenges for 2PP printing due to an intense bubbling phenomenon observed at the resist-substrate interface upon the commencement of printing. This bubbling led to the deformation of the printed microstructures and caused significant adhesion issues. Interestingly, this bubbling issue was considerably reduced when printing directly onto the chip frame using the same power settings, despite the identical coating layers. To overcome the challenges posed by the membrane substrate, a support structure was first printed directly on the chip frame before the effective lens structure was fabricated. This strategy not only mitigated the bubbling problem but also provided a more stable foundation for the printed structure. Consequently, a chip with a smaller membrane window was selected to ensure an appropriate support size for the CRL.

Before printing the CRL, the position of the FZP on the membrane was identified using the built-in microscope of the 3D printer, equipped with a 63× objective lens. The center of the FZP served as the reference point for the CRL printing process. Despite the resolution limitations of the light microscope, which is constrained by the wavelength of visible light, movements as small as 100 nm could be detected, allowing for precise alignment.

A commercial acrylate-based negative photo-resist (IP-S, Nanoscribe, Germany) was employed in the dip-in lithography mode, utilizing the 63× objective. The CRL consisted of 20 identical stacked parabolic lenses, each with an aperture of 100 µm, a height of 125 µm, and a radius of curvature at the parabola vertex of 20 µm, resulting in a virtual focal length of −95 mm, precisely matching the achromatic condition with the coupled FZP. The X-ray transmission rate of the CRL was estimated to be 37% based on a chemical formula of $C_{14}H_{18}O_7$ and a volumetric mass density of 1.2 g/cm^3 at 7.1 keV [34].

4.3. Experiments

4.3.1. Full-field transmission X-ray microscopy measurements

The full-field transmission X-ray microscopy (TXM) experiments were performed at the ANATOMIX beamline at the Synchrotron SOLEIL, France [25]. The X-ray energies used were 6.6 keV, 7.1 keV, 7.6 keV, and 8.1 keV. A monochromatic beam was produced by a Si(111) double-crystal monochromator, providing an energy resolution of $\Delta E/E = 10^{-4}$. X-rays were generated by a U18 cryogenic in-vacuum undulator and shaped using a series of slits and a diffractive condenser [35] (1.0 mm in diameter and 166 nm outermost zone width) to define the beam size at the sample position to approximately 0.04 mm × 0.04 mm. A diffuser was used to reduce the coherence of the beam, preventing coherence artifacts such as interference fringes and speckle patterns in the final images [36]. Samples were imaged using a full-field TXM setup. The detection system was a Hamamatsu Orca Flash 4.0 V2 camera with a CMOS sensor (2048 × 2048 pixels, 6.5 µm pixel size), a 10× objective (Mitutoyo) and a LuAG:Ce scintillator.

4.3.2. STXM and ptychography measurements

Scanning transmission X-ray microscopy and ptychographic X-ray imaging were performed at the cSAXS beamline of the Swiss Light Source (SLS), Paul Scherrer Institute, Switzerland.

In ptychography [20], a confined coherent illumination is used and the sample is raster-scanned in a way that neighboring illuminated areas partially overlap. At each scanning position, coherent diffraction patterns are recorded with an area detector in the far field. Iterative phase retrieval algorithms are then used to reconstruct the complex-valued image, with a resolution that can be better than the illumination size and than the step size in the scan. Owing to the diversity in the measured diffraction patterns coming from the overlapping illuminated areas, the reconstruction process is very robust, such that it also allows for the reconstruction of the complex-valued illumination [18]. This capability makes X-ray ptychography an ideal technique to characterize X-ray optics. As the complex-valued wavefront of the illumination is reconstructed, it can be propagated to different points along the optical axis to study the focusing behavior of the lens.

For both STXM and ptychographic scans, the energy was selected with a Si(111) double-crystal monochromator. The monolithic achromat was used in combination with a 100 µm aperture, and a 30 µm central stop, placed upstream of the lens, and a 20 µm order-sorting aperture, placed downstream. The lens was coherently illuminated, for which a secondary slit placed 12 m downstream of the source was set to a horizontal width of 20 µm.

For STXM, the sample was placed in the focal plane of the lens and scanned over an $18 \times 18 \mu m^2$ field of view with a step size of 150 nm. Diffraction patterns were recorded using a Pilatus 2M single-photon counting detector [37] with pixel size $172 \times 172 \mu m^2$ placed at a distance of 7273 mm downstream the sample, with an exposure time of 200 ms at each position. For the image processing, we integrated the intensity of the 400×400 pixels around the center of the beam.

For the ptychography measurements, the sample, placed close to the focal plane of the lens, was scanned over a 4×4 µm^2 field of view in a Fermat spiral pattern [38] with an average step size of 200 nm. In ptychography, the step size needs to be smaller than the size of the illumination to guarantee sufficient overlap between neighboring illuminated areas [39]. In our case, the illumination is larger than the 200 nm FWHM of the focused beam, due to the intensity distribution existing around the central focal spot, as observed in Figure S1c. Therefore, our ptychographic scans with a step size of 200 nm ensured sufficient overlap of neighboring illuminated regions, providing high-quality ptychographic reconstructions, as shown in Figure S1b. Diffraction patterns were recorded using the same Pilatus 2M detector, with a dwell time of 200 ms at each position.

Ptychographic reconstructions were performed using a selection of 400×400 pixels of the detector, resulting in a reconstructed pixel size ranging from 19.9 nm (6.6 keV) to 16.2 nm (8.1 keV). For the reconstructions, we used 300 iterations of the difference map algorithm followed by 400 iterations of the maximum likelihood algorithm [40], implemented in the PtychoShelves software package [41].

4.3.3. Fluorescence imaging

Fluorescence measurements were conducted at the microXAS beamline (X05LA) of the Swiss Light Source (SLS) [26]. The high-flux X-ray beam was generated using a U19 minigap in-vacuum undulator. The energy resolution was maintained at $\Delta E/E < 10^{-4}$ using a Si(111) double-crystal monochromator. The X-ray beam was shaped with a 100 µm upstream pinhole aperture, a 30 µm central stop, and a 20 µm order-sorting aperture.

The fluorescence energy scan was performed from 7 keV to 8.6 keV, with a 200 eV step size. Spatial scanning was carried out over a 100 µm × 100 µm field of view with a 0.5 µm step size. Fluorescence detection was performed using a single-element silicon drift detector (SDD; Ketek GmbH, Germany) with a 50 mm^2 active area.

Optics EXPRESS

Funding. Swiss Nanoscience Institute (16.01 ACHROMATIX); H2020 Marie Skłodowska-Curie Actions (884104); Agence Nationale de la Recherche (ANR-11-EQPX-0031).

Acknowledgment. We acknowledge the Paul Scherrer Institut, Villigen, Switzerland for provision of synchrotron radiation beamtime at the cSAXS beamline of the SLS under proposal 20212089 and microXAS beamline of the SLS under proposal 20220587. We acknowledge the Synchrotron SOLEIL for granted beamtime in the framework of proposal 20210898. ANATOMIX is an Equipment of Excellence (EQUIPEX) funded by the Investments for the Future program of the French National Research Agency (ANR), project NanoimagesX, grant No. ANR-11-EQPX-0031.

Disclosures. The authors declare no conflicts of interest.

Data availability. Data underlying the results presented in this paper are not publicly available at this time but may be obtained from the authors upon reasonable request.

Supplemental document. See Supplement 1 for supporting content.

References

1. D. Attwood, *Soft X-Rays and Extreme Ultraviolet Radiation* (Cambridge University, 1999), chap. 11.
2. P. W. Hawkes and J. C. H. Spence, eds., *Science of Microscopy* (Springer, 2007), chap. 20.
3. Y. Wang, W. Yun, and C. Jacobsen, "Achromatic Fresnel optics for wideband extreme-ultraviolet and X-ray imaging," Nature **424**(6944), 50–53 (2003).
4. G. K. Skinner, "Design and imaging performance of achromatic diffractive–refractive x-ray and gamma-ray Fresnel lenses," Appl. Opt. **43**(25), 4845–4853 (2004).
5. H. N. Chapman and S. Bajt, "High-resolution achromatic X-ray optical systems for broad-band imaging and for focusing attosecond pulses," Proc. R. Soc. A **477**(2251), 20210334 (2021).
6. A. Snigirev, V. Kohn, I. Snigireva, *et al.*, "A compound refractive lens for focusing high-energy X-rays," Nature **384**(6604), 49–51 (1996).
7. M. Young, "Zone Plates and Their Aberrations," J. Opt. Soc. Am. **62**(8), 972–976 (1972).
8. A. Kubec, M.-C. Zdora, U. T. Sanli, *et al.*, "An achromatic X-ray lens," Nat. Commun. **13**(1), 1305 (2022).
9. U. T. Sanli, G. Rodgers, M.-C. Zdora, *et al.*, "Apochromatic X-ray focusing," Light: Sci. Appl. **12**(1), 107 (2023).
10. S. Ali and C. Jacobsen, "Effect of tilt on circular zone plate performance," J. Opt. Soc. Am. A **37**(3), 374–383 (2020).
11. R. Celestre, T. Roth, C. Detlefs, *et al.*, "Tilting refractive x-ray lenses for fine-tuning of their focal length," Opt. Express **31**(5), 7617–7631 (2023).
12. S. Gorelick, V. A. Guzenko, J. Vila-Comamala, *et al.*, "Direct e-beam writing of dense and high aspect ratio nanostructures in thick layers of PMMA for electroplating," Nanotechnology **21**(29), 295303 (2010).
13. S. Gorelick, J. Vila-Comamala, V. A. Guzenko, *et al.*, "High-efficiency fresnel zone plates for hard X-rays by 100 keV e-beam lithography and electroplating," J. Synchrotron Radiat. **18**(3), 442–446 (2011).
14. A. K. Petrov, V. O. Bessonov, K. A. Abrashitova, *et al.*, "Polymer X-ray refractive nano-lenses fabricated by additive technology," Opt. Express **25**(13), 14173–14181 (2017).
15. H. Wang, W. Zhang, D. Ladika, *et al.*, "Two-photon polymerization lithography for optics and photonics: Fundamentals, materials, technologies, and applications," Adv. Funct. Mater. **33**(39), 2214211 (2023).
16. N. Bobroff, "Position measurement with a resolution and noise-limited instrument," Rev. Sci. Instrum. **57**(6), 1152–1157 (1986).
17. R. E. Thompson, D. R. Larson, and W. W. Webb, "Precise nanometer localization analysis for individual fluorescent probes," Biophys. J. **82**(5), 2775–2783 (2002).
18. P. Thibault, M. Dierolf, A. Menzel, *et al.*, "High-Resolution Scanning X-ray Diffraction Microscopy," Science **321**(5887), 379–382 (2008).
19. O. Bunk, M. Bech, T. H. Jensen, *et al.*, "Multimodal x-ray scatter imaging," New J. Phys. **11**(12), 123016 (2009).
20. F. Pfeiffer, "X-ray ptychography," Nat. Photonics **12**(1), 9–17 (2018).
21. J. Vila-Comamala, A. Diaz, M. Guizar-Sicairos, *et al.*, "Characterization of high-resolution diffractive X-ray optics by ptychographic coherent diffractive imaging," Opt. Express **19**(22), 21333–21344 (2011).
22. A. Menzel, C. M. Kewish, P. Kraft, *et al.*, "Scanning transmission X-ray microscopy with a fast framing pixel detector," Ultramicroscopy **110**(9), 1143–1147 (2010).
23. W. Chao, B. D. Harteneck, J. A. Liddle, *et al.*, "Soft X-ray microscopy at a spatial resolution better than 15 nm," Nature **435**(7046), 1210–1213 (2005).
24. B. Niemann, V. Sarafis, D. Rudolph, *et al.*, "X-ray microscopy with synchrotron radiation at the electron storage ring BESSY in Berlin," Nucl. Instrum. Methods Phys. Res., Sect. A **246**(1-3), 675–680 (1986).
25. M. Scheel, J. Perrin, F. Koch, *et al.*, "Current status of hard X-ray nano-tomography on the transmission microscope at the ANATOMIX beamline," J. Phys.: Conf. Ser. **2380**(1), 012045 (2022).
26. C. N. Borca, D. Grolimund, M. Willimann, *et al.*, "The microXAS beamline at the swiss light source: Towards nano-scale imaging," J. Phys.: Conf. Ser. **186**, 012003 (2009).
27. M. J. Pushie, I. J. Pickering, M. Korbas, *et al.*, "Elemental and Chemically Specific X-ray Fluorescence Imaging of Biological Systems," Chem. Rev. **114**(17), 8499–8541 (2014).
28. I. Mohacsi, P. Karvinen, I. Vartiainen, *et al.*, "High-efficiency zone-plate optics for multi-keV X-ray focusing," J. Synchrotron Radiat. **21**(3), 497–501 (2014).

Optics EXPRESS

29. I. Mohacsi, I. Vartiainen, M. Guizar-Sicairos, *et al.*, "Fabrication and characterization of high-efficiency double-sided blazed x-ray optics," Opt. Lett. **41**(2), 281–284 (2016).
30. U. T. Sanli, H. Ceylan, I. Bykova, *et al.*, "3D Nanoprinted Plastic Kinoform X-Ray Optics," Adv. Mater. **30**(36), 1802503 (2018).
31. X. Tong, Y. Chen, Z. Xu, *et al.*, "Trapezoid-kinoform zone plate lens – a solution for efficient focusing in hard X-ray optics," J. Synchrotron Radiat. **29**(2), 386–392 (2022).
32. V. Aristov, M. Grigoriev, S. Kuznetsov, *et al.*, "X-ray refractive planar lens with minimized absorption," Appl. Phys. Lett. **77**(24), 4058–4060 (2000).
33. M. Malinauskas, M. Farsari, A. Piskarskas, *et al.*, "Ultrafast laser nanostructuring of photopolymers: A decade of advances," Phys. Rep. **533**(1), 1–31 (2013).
34. B. L. Henke, E. M. Gullikson, and J. C. Davis, "X-ray interactions: Photoabsorption, scattering, transmission and reflection E = 50-30,000 eV, Z = 1-92," At. Data Nucl. Data Tables **54**(2), 181–342 (1993).
35. K. Jefimovs, J. Vila-Comamala, M. Stampanoni, *et al.*, "Beam-shaping condenser lenses for full-field transmission X-ray microscopy," J. Synchrotron Radiat. **15**(1), 106–108 (2008).
36. S. C. Irvine, K. S. Morgan, Y. Suzuki, *et al.*, "Assessment of the use of a diffuser in propagation-based x-ray phase contrast imaging," Opt. Express **18**(13), 13478–13491 (2010).
37. B. Henrich, A. Bergamaschi, C. Broennimann, *et al.*, "PILATUS: A single photon counting pixel detector for X-ray applications," Nucl. Instrum. Methods Phys. Res., Sect. A **607**(1), 247–249 (2009).
38. X. Huang, H. Yan, R. Harder, *et al.*, "Optimization of overlap uniformness for ptychography," Opt. Express **22**(10), 12634–12644 (2014).
39. O. Bunk, M. Dierolf, S. Kynde, *et al.*, "Influence of the overlap parameter on the convergence of the ptychographical iterative engine," Ultramicroscopy **108**(5), 481–487 (2008).
40. P. Thibault and M. Guizar-Sicairos, "Maximum-likelihood refinement for coherent diffractive imaging," New J. Phys. **14**(6), 063004 (2012).
41. K. Wakonig, H.-C. Stadler, M. Odstrčil, *et al.*, "*PtychoShelves*, a versatile high-level framework for high-performance analysis of ptychographic data," J. Appl. Crystallogr. **53**(2), 574–586 (2020).